Granular buoyancy in the context of segregation of single large grains in dense granular shear flows

M. P. van Schrojenstein Lantman●, K. van der Vaart●, S. Luding●, and A. R. Thornton●*
Department of Thermal and Fluid Engineering, Faculty of Engineering Technology, MESA+,
University of Twente, P.O. Box 217, 7500 AE Enschede, The Netherlands

Modeling of particle-size segregation in dense granular flows could benefit from a better understanding of the segregation behavior of individual large grains that are surrounded by smaller grains. In a previous study, the force in the direction of segregation experienced by such a particle was measured and decomposed into a modified Archimedean buoyancy force and a segregation lift force. Here we present a new micromechanical analysis of this granular buoyancy force that connects the microscale contact behavior to the macroscopic force, thereby lending further support to its validity. In the process of this validation we uncover evidence linking the average surface contact density on a grain to the scaling of the buoyancy force with its size. Our findings support the use of the existing Voronoi approximation for calculation of the granular buoyancy force and substantiate the decomposition of the net force into buoyancy and segregation lift. Ultimately, these insights will aid development of new models for size segregation by closely linking micro and macro behavior.

I. INTRODUCTION

Granular mixtures that consist of different-sized grains have the ability to segregate when agitated, a complex mechanical process that leads to the spatial separation of grains by their size [1–4]. Different forms of agitation of granular mixtures, such as shearing [5], shaking [6], or vibration [7–11], can lead to different forms or types of size segregation. In dense granular flows [12,13], driven by gravity or externally applied shear, size segregation most commonly consist of larger grains rising against gravity towards the flow's free-surface whilst smaller grains sink to the bed. This process has been intensively studied (see, e.g., Refs. [14–31]), its relevance ranging from geophysical mass flows to industrial handling of powders and grains.

The predictive power of current state-of-the-art modeling approaches [17,32–37] is acurate under the condition that the small and large-particle concentrations (solid or volume fractions) in a mixture are relatively similar [21]. With modifications that account for size-segregation asymmetry [38,39] models do perform better for more unequal concentrations. However, predictions remain inaccurate at very low large-particle concentrations, where large grains are surrounded by many smaller grains and segregation progresses slowly [40]. Increasing our understanding and modeling capabilities of size segregation in this lower limit is relevant because both during the process of segregation as

---

*a.r.thornton@utwente.nl

well as after reaching a steady state local regions of very low large-particle concentration occur and persist, even in mixtures where globally the volume-ratio between small and large grains is comparable [38,41,42].

In an effort to understand the low large-particle concentration limit a number of studies have addressed the segregation behavior of a single large particle in a dense shear flow composed of smaller grains [42–46]. Such a particle is typically referred to as an intruder and is known to rise towards the flow's free-surface. Despite relevant progress no common consensus has been reached about the origin, measurement and modeling of the forces responsible for rising of such an intruder. To illustrate this point we will briefly recap the recent advances.

Guillard *et al.* [43] introduced a method that addressed two of the main challenges that arise when trying to measure the segregation lift force on a single large intruder in simulations. The first issue is as follows. If, as a result of some unknown segregation lift force, a large grain rises towards the flow's free-surface the net vertical force, as measured from the particle contacts, is on average exactly equal and opposite to the gravitational force [45]. This would imply that no lift force exists. However, it stands to reason that if there exists a force in excess of the gravitational force, i.e., the total vertical contact force is larger than gravity, the intruder will rise but it will also accelerate. Such an acceleration would naturally be counteracted by a drag force. Consequently, the net vertical contact force would be lowered until it is once again in balance with gravity. This reasoning suggests that measuring (on average) any force in excess of gravity is impossible for a freely rising intruder. The second issue is one of time averaging. To accurately measure forces in this problem long time-averaging is important because on the particle-scale fluctuations are strong. The method introduced by Guillard *et al.* [43] solved both of these issues. In this method the intruder is attached to a virtual spring that produces a force in the vertical direction only if the intruder moves away from the anchor point. This prevents it from continuously rising and a drag force from building up. Thus, with the spring attached the total vertical contact force can outgrow gravity and the excess force can be measured (see the schematic in Figure 1). It also allows for long time-averaging because the intruder never reaches the flow's free-surface.

A question that arises with this particle-on-a-spring method is whether the force in excess of gravity is the segregation lift force. Guillard *et al.* [43] side-stepped this question by modeling the total vertical contact force, which is partly composed of the excess force. Their model consists of scaling laws that depend on the spatial derivatives of the pressure and shear stress, and it can accurately predict the direction of segregation in various flow configurations. Thereafter Jing *et al.* [46] also considered the total vertical contact force. With a fitting equation they captured the dependence of this force on the size ratio between the intruder and bulk grains. They demonstrated the generality of the equation they retrieved by predicting the upward and downward segregation of intruders with different sizes and densities, as reported by Félix and Thomas [47], in different flow geometries. Sinking of intruders can occur if their density is higher than that of the bulk grains. It is unclear, however, if this is due to a downward (in the direction of gravity) directed segregation force, or a buoyancy effect.

It should be mentioned that Staron [45] argued that the force in excess of gravity that arises using the particle-on-a-spring method is an artefact. For this reason she studied freely rising intruders, found that the total vertical contact force balanced gravity and concluded that the lift force on a free intruder has to be very small. She went on to model the rising of the intruder via positive force fluctuations and an asymmetry in the ease at which an object in a granular flow can be pushed downwards versus upwards [48].

While Guillard *et al.* [43] and Jing *et al.* [46] considered the total vertical force to model segregation of single large intruders, Van der Vaart *et al.* [44] attempted a force decomposition to isolate a distinct segregation lift force. Their goal was to shed light on its origin. The approach they took was to subtract from the total vertical contact force a newly developed granular buoyancy force. The inspiration for this decomposition came from measurements of the pressure field surrounding the intruder that showed a deviation from a hydrostatic pressure when the intruder was larger than the bulk grains. Van der Vaart *et al.* [44] argued that the hydrostatic component of the pressure
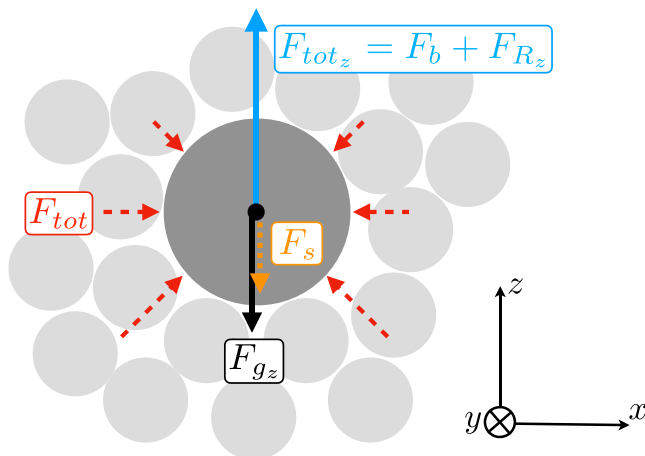
FIG. 1. Schematic of the problem considered. A single intruder in a sheared granular flow. Several forces are depicted. The total contact force F_{tot} (in red) results from all particle contacts. The vertical component of the gravitational force F_{g_z} (in black) is set by the size of the intruder. For F_{tot} we develop a model and subsequently decompose it into a buoyancy force F_b (in blue) and remaining forces F_R, of which we show in this schematic the vertical component F_{R_z} (in blue). Together F_b and F_{R_z} make up the vertical component of the total force F_{tot_z} (in blue). The force F_{R_z} is composed of the segregation lift force [44] but possibly other forces as well. Last, there is the spring force F_s (in orange), which is applied artificially in our simulation and adapts itself to balance the vertical forces. Its function is only to prevent a large intruder from rising upwards through the process of segregation thus allowing for long time-averaging. The presence of the spring force does not influence our theoretical analysis.

cannot be held responsible for the lift force as it is also present when the intruder is identical to the bulk particles and not segregating. Hence, the lift force should be associated with the deviation of the pressure from hydrostatic. Therefore, the buoyancy force, which is the result of the hydrostatic pressure, needs to be subtracted to obtain the lift force. The approach proved valuable as it revealed a potential origin for the lift force. The lift force is a Saffman-like force [49] in that it correlates with a velocity difference in the downstream direction between the intruder and the bulk. This velocity "lag" of a segregating intruder was discovered in that same study [44]. The findings reported in Ref. [44] also demonstrate that the lift force is in fact larger than the force in excess of gravity that is measured through the particle-on-a-spring method. The reason being that granular buoyancy is smaller than the gravitational force acting on large intruders. This finding has since been supported by theoretical work [50].

The works of Jing *et al.* [46] and Staron [45] followed that of Van der Vaart *et al.* [44], indicating that there are still open-questions about the origin of the segregation lift force with differing ideas presented. One reason for this could be that the new granular buoyancy force [44] (which plays such a critical role in isolating the segregation lift force) is currently not supported by any physical or micromechanical understanding or derivation. Instead, its mathematical form, which makes use of the Voronoi volume of the intruder, was chosen because it scales with the size ratio S between intruder and the bulk grains and recovers the theoretically correct buoyancy force in two limits of S; for an infinitely large intruder and for an intruder that is identical in size to the bulk grains. Between these two limits this Voronoi-based granular buoyancy force can only be considered as an approximation. We suspect that more firmly establishing the granular buoyancy force introduced in Ref. [44] will help towards reaching a consensus on the topic of the segregation lift force in dense granular flows.

In this study we address the lack of physical or micromechanical understanding of the granular buoyancy force on a spherical grain introduced in Ref. [44]. In doing so we aim to more firmly

establish this granular buoyancy force and in turn support the method of measuring the segregation lift force [44]. We use a straightforward theoretical methodology to split the contact structure on the intruder from the force structure and derive a micromechanical definition for granular buoyancy. This definition makes use of anisotropic angular distribution functions for contacts and forces, as well as an average contact density and an average contact force. We validate this new approach through numerical simulations and find that it compares favourably with the granular buoyancy introduced in Ref. [44] that makes use of the Voronoi volume of the intruder. Moreover, we uncover evidence linking the scaling of granular buoyancy with the intruder size ratio to a change in surface contact density, thereby providing additional fundamental insights into granular buoyancy. Figure 1 shows a schematic of the problem and the relevant forces.

II. THEORETICAL BACKGROUND

Before discussing our findings we will outline the necessary theoretical background and developments in fluid and granular buoyancy in this section.

A. Classical buoyancy: Archimedes' principle

Before we consider a granular material we will begin with Archimedes' principle for objects submerged in a Newtonian fluid. Archimedes' principle states that such an object experiences a force, called the buoyancy force, that is proportional to the weight of the displaced fluid, the origin of which is the weight of the fluid pushing on the object. With the horizontal forces balancing and the fluid underneath the object exerting a stronger force as a result of the higher pressure, the net buoyant force is in the opposite direction of gravity. In a normal fluid, as long as the density of the object is equal to that of the fluid the buoyancy force is balanced by the gravitational force acting on the object.

Given the stress tensor in a Newtonian fluid [51] $\boldsymbol{\sigma} = \boldsymbol{\tau} - p\boldsymbol{I}$, the total force on a submerged object can be calculated by integrating the stress over its surface area,

$$F = \int_{A_p} \boldsymbol{\sigma} \boldsymbol{n} dA, \tag{1}$$

where $\boldsymbol{n}$ is the normal outward unit vector. Here, the object's surface area is A_p. The component of the total force that is the buoyancy force $\boldsymbol{F}_b$ is defined as the integral of the pressure over the object's surface area, or the integral of the gradient of the pressure over the object's volume,

$$\boldsymbol{F}_b \equiv \int_{A_p} -p^R \boldsymbol{n} dA = -\int_{V_p} \nabla p^R dV, \tag{2}$$

where the divergence theorem is used to obtain the volume integral. Here, the object's volume is V_p. The pressure has to be taken in the absence of the object in the so-called undisturbed reference flow, here referred to with the superscript R.

B. Granular buoyancy for $S \to \infty$

A straightforward and established translation of the classical Archimedean buoyancy force to a particle in a dense granular flow uses the granular hydrostatic pressure,

$$p_h = \phi_b \rho g_z [H - z], \tag{3}$$

where ϕ_b is the solids or volume fraction of the bulk, ρ is the density of the bulk particles, g_z is the vertical component of the gravitational acceleration, H is the flow depth and z is the vertical position of the intruder. Since the pressure is equal to $p_h = -\sigma_{zz}^R = -(\tau_{zz}^R - p^R)$, the stress anisotropy that exists in granular flows is accounted for in the hydrostatic pressure [52]. With the derivatives of the pressure in the x and y direction being zero it follows from Eq. (2) that the granular buoyancy

force is

$$F_{b,\infty} \equiv -\int_{V_p} \frac{\partial p_h}{\partial z} dV = \phi_b \rho V_p g_z.$$ (4)

The subscript ∞ refers to the theoretical limit $S \to \infty$ where the size ratio between intruder and bulk particles goes to infinity and this definition is expected to hold true. When the size ratio goes to infinity the bulk particles are so small that they can be treated as a fluid with a density $\phi_b \rho$, essentially yielding the classic Archimedean buoyancy force. The only experimental verification of this definition for a granular system to our knowledge was reported by Huerta *et al.* [53], who studied large intruders ($S > 8$), of lesser density [54] compared to the bulk particles, rising in a horizontally shaken granular fluid. With this form of agitation the Brazil nut segregation mechanism [6,55] is absent, therefore the upward force can safely be attributed to buoyancy. Huerta *et al.* [53] found this force to be equal to Eq. (4). Because it is unknown how to turn off the shear induced segregation lift force, buoyancy forces have not been measured in isolation in dense shear-driven granular flows (except for when the intruder is identical to the bulk particles). When considering the buoyancy force in other types of systems, such as the fluidization of static granular materials, this pressure gradient causes additional phenomena [56,57].

C. Granular buoyancy for $S = 1$

A second limit for which a granular buoyancy can be defined is at $S = 1$, where buoyancy must balance gravity if the intruder has the same density as the bulk particles. The definition in Eq. (4) cannot be used in this limit since it differs from the gravitational force. The most reasonable approach to resolve this issue is as follows. Since the hydrostatic pressure is defined over the entire volume, that is, also in the void space, integration of the pressure can be done over an effective volume that includes this void space. This effective volume V_{eff} should be the total volume of the mixture divided by the number of particles it contains. In this way the void space is equally divided over all particles, which is required at $S = 1$ because all particles are identical. Given the definition of the bulk volume fraction $\phi_b = NV_p/V_{\text{tot}}$, the effective volume can be expressed as $V_{\text{eff}} = V_{\text{tot}}/N = V_p/\phi_b$. It is plain to see that integrating the pressure gradient over this volume removes the factor ϕ_b, yielding a buoyancy force that equals gravity,

$$F_{b,1} \equiv -\int_{V_{\text{eff}}} \frac{\partial p_h}{\partial z} dV = \rho V_p g_z = F_g,$$ (5)

where the subscript "1" refers to the limit of $S = 1$.

D. Voronoi-based approximation to granular buoyancy

A natural approach to satisfy both the limit at $S = 1$ and at $S \to \infty$ with one buoyancy definition is to use an effective volume for integration that has an appropriate size-ratio dependence. For this purpose van der Vaart *et al.* [44] introduced the Voronoi volume of the intruder particle $\mathcal{V}$, which leads to a buoyancy force of the form

$$F_{b,\mathcal{V}} \equiv -\int_{\mathcal{V}} \frac{\partial p_h}{\partial z} dV = \phi_b \rho \mathcal{V} g_z.$$ (6)

This definition theoretically satisfies both limits. For a homogeneous mixture at $S = 1$, each particle has identical values for V_p and (on average) for $\mathcal{V}$. As such, $\mathcal{V} = V_p/\phi_b$, and thus $F_{b,\mathcal{V}} = F_{b,1}$. For $S \to \infty$ the bulk particles will be so small that the intruder Voronoi volume fits closely to its surface, in other words $\mathcal{V} \to V_p$, and thus $F_{b,\mathcal{V}} = F_{b,\infty}$.

The Voronoi-based granular buoyancy is a simple approach that defines a granular buoyancy force for grains within the two size ratio limits, based on purely geometrical arguments [44]. It is unknown whether it guarantees physical correctness between the two limiting points. For that reason we have performed the micromechanical derivation in this study.

E. Intermezzo: Granular buoyancy versus gravity

Per the definition in Eq. (6), for size ratios above unity the granular buoyancy is smaller, by a factor of ϕ_b, than the gravitational force $F_g = \rho V_p g_z$ on an intruder with identical density as the bulk particles. This has two implications. First, in the absence of a segregation lift force [43,44,46] large intruders should sink instead of rise against gravity as they are known to do in dense granular flows. Second, taking the vertical force in excess of gravity to be the segregation lift force is incorrect and underestimates the latter.

Studies on very large intruders in dense granular flows ($S > 5$) have indeed reported that these can sink instead of rise [47,58]. A possible explanation is that the lift force changes sign. The more likely scenario, however, is that the lift force eventually decreases, and with the buoyancy being less than gravity the large intruder will sink.

Recently two important pieces of evidence were reported. In numerical simulations, van der Vaart *et al.* [44] set the contact friction of a large intruder to zero and observed that the gravitational force was bigger than the vertical contact force, which resulted in the intruder sinking. Thus, demonstrating that the granular buoyancy force does not balance gravity for $S > 1$. The second piece of evidence supports a decreasing segregation lift force at size ratios bigger than 2. Namely, for a normal frictional large intruder van der Vaart *et al.* [44] subtracted the granular buoyancy force from the vertical contact force and found that the remainder, i.e., the segregation lift force, first increased with intruder size ratio and then decreased after $S \approx 2$.

A recent theoretical derivation of granular buoyancy [50], that uses the equation of state of hard sphere mixtures [59], has shown good agreement with the simulation results reported in Ref. [44].

III. METHODS

A. Simulation method and setup

We simulate a gravity driven granular flow down an inclined plane (chute flow) composed of bulk particles that are all identical and a single intruder particle. The inclination angle $\theta_c = 22°$ and we apply periodic boundaries in the x and y directions. This geometry was chosen because it produces a velocity field which is shearing in only one plane, the xz plane. Second, this is a well studied and understood system, see Refs. [52,60,61] and references therein.

We use the discrete particle method (DPM), also known as the discrete element method. The system is nondimensionalized such that the nondimensional bulk particle diameter $d = 1$, density $\rho = 6/\pi$, and the gravitational acceleration $g = 1$. The simulation box has a size $(L_x, L_y, L_z) = (20, 8.9, 40)d$. The gravitational acceleration is given by $\boldsymbol{g} = [\sin(\theta_c), 0, -\cos(\theta_c)]$. A rough bottom is composed of particles, with a diameter of $1.7d$, slightly larger than the bulk particles. Details for the creation method of the rough bottom can be found in Weinhart *et al.* [61].

There are roughly 6000 dry frictional bulk particles. This yields an average flow height of $h \approx 30d$. Contacts between particles are modeled using a linear spring-dashpot model [52,62] with linear elastic and linear dissipative contributions for the normal forces between particles. Particle properties and contact parameters are given in Table I. The stiffness and dissipation of the contact laws are computed through the analysis of two colliding particles [63]. The tangential, sliding and rolling friction between bulk particles are all equal to the friction coefficient μ_b in Table I. The friction between intruder and bulk particles is taken similar to μ_b. Simulations are performed by the open-source software package MercuryDPM [64–66].

The single intruder particle with size ratio $S = d_p/d$ is introduced in the flow at a height of $z_{p,0} = 23$. To prevent the intruder from rising continuously, a virtual restoring spring is introduced in the z direction, whilst it can freely flow in the x and y directions. This method was introduced by Guillard *et al.* [43]. The spring stiffness of the restoring spring is set to $k_s = 20$. We verified that the flow properties without an intruder present conform with the literature.

TABLE I. Dimensionless particle properties and contact model parameters. Contact duration and restitution coefficient set the stiffness and dissipation of the particles; see Luding [63].

Parameter	Symbol	Value
Bulk particle diameter	d	1.0
Intruder size ratio	S	1.0–3.2
Intruder particle diameter	d_p	1.0–3.2
Particle density	ρ	$\pi/6$
Restitution coefficient	e_r	0.1
Contact duration	t_c	0.005
Friction	μ_b	0.5

B. Analysis of simulations

To measure and analyze forces and contacts on the surface of the intruder we tessellate its surface with mesh elements. Here we use a spherical coordinate system with (r, θ, ϕ), respectively, the radial, azimuthal, and polar direction, where $\theta \in [0, 2\pi)$ and $\phi \in [0, \pi]$. The angles are uniformly discretized with $\Delta\theta = 2\pi/n_\theta$ and $\Delta\phi = \pi/n_\phi$, where n_θ and n_ϕ are the number of elements in the θ and ϕ direction, respectively. The surface area of a mesh element is denoted by ΔA_{ij}, where the indices i and j indicate the mesh coordinates θ_i and ϕ_j. To obtain good statistical data, $N_t = 3400$ time snaps were used with 9724 contacts for the $S = 1$ case. A grid of $n_\theta = 20$ and $n_\phi = 10$ resulted in a detailed yet reasonably smooth surface. Larger sized intruders encounter more contacts due to increasing coordination number improving the statistical results.

IV. RESULTS

A. Contact structure and force structure

To gain microscale insights into the granular buoyancy force we investigate the structural changes around the intruder when the size ratio increases. Although the interaction between particles is of a discrete nature, we consider a situation where the flow is in a steady state and we average over a long time-window such that a continuum approach is allowed; the many contacts that occur lead on average to a net force. This average total contact force on the intruder (see Fig. 1) can be expressed as

$$\boldsymbol{F}_{\text{tot}} = \int_{A_p} \frac{d\boldsymbol{F}}{dA} dA, \tag{7}$$

where $d\boldsymbol{F}$ is the average force on an infinitesimal surface element dA of the intruder and A_p is its surface area. By taking a similar approach to Rothenburg and Bathurst [67], the total force on the surface of the intruder can be split into a force structure and a contact structure. This approach has been used to study bulk behavior of granular materials in 2D [68,69] and 3D [70] for constitutive modeling. Applying the chain rule yields

$$\boldsymbol{F}_{\text{tot}} = \int_{A_p} \frac{d\boldsymbol{F}}{dC} \frac{dC}{dA} dA = \int_{A_p} \boldsymbol{F}_c E \, dA, \tag{8}$$

where dC is the number of contacts on an infinitesimal surface element dA,

$$\boldsymbol{F}_c \equiv \frac{d\boldsymbol{F}}{dC} \tag{9}$$

is the average local force per contact, called the force structure, and

$$E \equiv \frac{dC}{dA} \tag{10}$$

is the average local number of contacts per surface area, called the contact structure. Both the force structure and contact structure are orientation dependent, i.e., dependent on the location on the intruder surface. Integrating the contact structure over the surface area yields the coordination number $\mathcal{Z}$,

$$\int_{A_p} E dA = \int_{A_p} \frac{dC}{dA} dA = \int_0^{\mathcal{Z}} dC \equiv \mathcal{Z}. \tag{11}$$

Next, we rewrite the total force, Eq. (8), in terms of normalized angular distribution functions for the contacts and contact forces. We write the contact structure as

$$E = c_\rho P_E, \tag{12}$$

where P_E is an angular (probability) distribution function that is normalized to one, and c_ρ is the average number of contacts per surface area

$$c_\rho \equiv \mathcal{Z}/A_p, \tag{13}$$

which we will refer to as the contact density.

To rewrite the force structure in terms of an angular distribution function we first split the former into a force magnitude F_c and contact vector $\boldsymbol{n}_c$,

$$\boldsymbol{F}_c \equiv F_c \boldsymbol{n}_c, \tag{14}$$

where F_c is an orientation dependent scalar. Normalization of F_c by the average force per contact $\bar{F}_c$ yields the normalized angular (probability) distribution function of the contact force

$$P_{F_c} \equiv \frac{F_c}{\bar{F}_c}. \tag{15}$$

Thus, the force structure can be written as

$$\boldsymbol{F}_c = \bar{F}_c P_{F_c} \boldsymbol{n}_c. \tag{16}$$

It is possible to further decompose $\boldsymbol{n}_c$ into tangential and normal components, but for our analysis of the buoyancy force we believe this is not required; both the tangential and normal component can contribute to the vertical component of the contact force which is the buoyancy force.

Finally, substituting Eqs. (12) and (16) in Eq. (8) yields

$$\boldsymbol{F}_{\text{tot}} = \bar{F}_c c_\rho \int_{A_p} P_{F_c} P_E \boldsymbol{n}_c dA. \tag{17}$$

By construction both $\bar{F}_c$ and c_ρ are orientation independent scalars that only depend on S. All orientation dependence is captured in the angular distribution functions. With this micromechanical definition of the total contact force we are now able to define a buoyancy force.

B. Micromechanical definition for granular buoyancy

Our next step is to decompose the total contact force [Eq. (17)] into the granular buoyancy force, which we know acts in the vertical direction, and the remaining force composed of lift and drag forces in which we are not interested presently. To do so we must first realize that whilst we can decompose forces, we can not decompose contacts. Hence, the contact structure will have to remain intact. So what we are left with to decompose is the angular distribution function of the forces P_{F_c} and the average contact force $\bar{F}_c$.

To proceed we make the following assumptions that follow from the ansatz that buoyancy arises due to the weight of the fluid pushing on the intruder:

(1) At $S = 1$ no segregation occurs and the buoyancy force is in equilibrium with the gravitational force, therefore the vertical contact force is equal to the buoyancy force;

(2) The hydrostatic pressure is linear in depth, therefore the buoyancy component of individual contact forces has to be (on average) linear in depth;

(3) The hydrostatic pressure is independent of intruder size, therefore the buoyancy component of individual contact forces has to be (on average) independent of intruder size.

Assumptions 2 and 3 specifically are consequences of the ansatz that buoyancy arises from the weight of the fluid—which for real fluids is the established origin of buoyancy. Since it is a priori impossible to know for $S > 1$ what the buoyancy component of individual contact forces is, assumptions 2 and 3 can only be verified in a flow where no vertical drag or lift forces act on the intruder.

The preceding assumptions lead us towards a solution where we (i) introduce a linear dependence on z, (ii) take $\bar{F}_c$ at $S = 1$, and (iii) take the component of P_{F_c} at $S = 1$ that is linear in depth. The decomposition of the force structure into a buoyancy and nonbuoyancy is, thus,

$$\bar{F}_c P_{F_c} = \bar{F}_{c,1} b_{z,1} z + R(S), \tag{18}$$

where $\bar{F}_{c,1} \equiv \bar{F}_c(S = 1)$, and $b_{z,1}$ is the magnitude of the linear vertical component of the angular distribution of forces at $S = 1$. We obtain the value of this coefficient from a fit to the measured distribution (see Appendix B). The $R(S)$ term is the remainder of the force structure, which will have a dependency on S (among others) and can be attributed to other mechanisms, such as drag and lift. Integration of $R(S = 1)$ should be zero which we verify in the next section.

Plugging the decomposition of the force structure [Eq. (18)] into the total force [Eq. (17)] and accounting for the fact that the buoyancy force acts along the direction of the pressure gradient, i.e., the vertical direction, we obtain

$$\boldsymbol{F}_{\text{tot}} = F_{b,\delta} \boldsymbol{e}_z + \boldsymbol{F}_R, \tag{19}$$

where the micromechanical definition for the granular buoyancy force is

$$F_{b,\delta} = \bar{F}_{c,1} b_{z,1} c_\rho(S) \int_{A_p} z P_E(S) \boldsymbol{n}_c \cdot \boldsymbol{e}_z dA, \tag{20}$$

and $\boldsymbol{F}_R$ encompasses all other forces. The subscript δ is used to distinghuish the micromechanical approach from the Voronoi-based buoyancy $F_{b,\mathcal{V}}$ and from the two definitions of buoyancy in the limits of S. The buoyancy force depends on S through the contact structure and possibly also through the contact vector $\boldsymbol{n}_c$.

C. Verification

We compare the micromechanical buoyancy force [Eq. (20)] to the Voronoi-based approximation [Eq. (6)] and verify it against the limits at $S = 1$ and $S \to \infty$. For this purpose we plot both approaches as a function of size ratio and nondimensionalise them by $F_{b,\infty}$. After this nondimensionalization, if the buoyancy force satisfies the correct limits, it should tend to unity for large S and to $1/\phi_b$ for $S = 1$. A second important aspect of nondimensionalization is that it divides out the dependency on the diameter of the intruder, leaving only the size ratio dependency. To calculate $F_{b,\delta}(S)$ we use measurements for the contact structure (see Appendix B 2), contact density and contact vector, whilst the values for $b_{z,1}$ and $\bar{F}_{c,1}$ are obtained from the fit to the angular force distribution (see Appendix B). To calculate $F_{b,\mathcal{V}}(S)$ the average intruder Voronoi volume is measured.

Figure 2 shows the two nondimensionalized buoyancy force definitions. The Voronoi-based buoyancy, which after normalization simplifies to $\mathcal{V}/V_p$, satisfies the two limits by construction (see Sec. II D). The micromechanical definition has at $S = 1$ a value of roughly $1.05/\phi_b$, which is
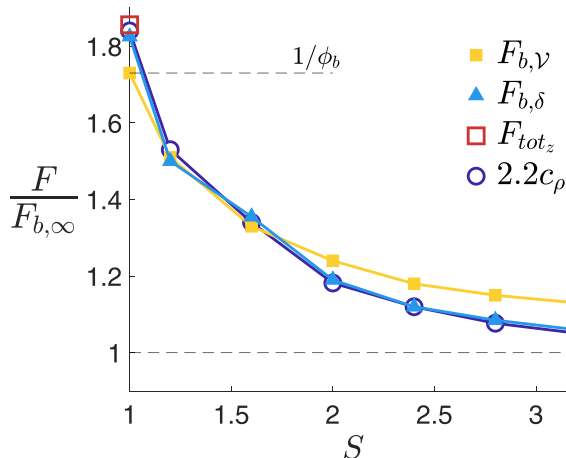
FIG. 2. The micromechanical buoyancy $F_{b,\delta}$, the Voronoi-based buoyancy $F_{b,\mathcal{V}}$, and the measured vertical component of the total contact force F_{tot_z} at $S = 1$, all nondimensionalized by $F_{b,\infty}$. Since the vertical contact force increases with S we plot it for $S = 1$ only, where it is expected to be equal to the buoyancy force. The upper dashed line corresponds to $1/\phi_b$ and the lower dashed line to 1. These are the two physical limits of the buoyancy at $S = 1$ and $S \rightarrow \infty$, given by Eqs. (5) and (4), respectively. The contact density c_ρ multiplied with an empirical scaling factor of 2.2 (and not normalized) is also shown.

slightly above the expected value $1/\phi_b$. The reason for this difference is likely related to force fluctuations which are much stronger for $S = 1$. The correct continuum limit is probably reached when averaging over a very long time period. The micromechanical definition does match up correctly with the vertical component of the total contact force F_{tot_z} measured at $S = 1$, thereby verifying our assumption that integration of $R(S)$ yields zero at $S = 1$. This also supports our choice to use $b_{z,1}$. For increasing S the micromechanical definition approaches, seemingly asymptotically, towards unity, in agreement with the expected limit. The Voronoi approximation compares favourably with the micromechanical definition, and the only notable difference is that at large S the Voronoi approximation slightly over estimates the buoyancy force, despite reaching the correct limit.

An important insight is revealed when comparing the size-ratio dependence of the normalized micromechanical definition for buoyancy to a measurement of the contact density $c_\rho(S)$. If multiplied with a proportionality factor of 2.2 the contact density practically overlaps with the normalized buoyancy force, thus demonstrating that the latter's dependency on size ratio can be attributed entirely to the contact density.

A simple geometrical analysis in the following section will explain why the contact density decreases with intruder size ratio.

D. Contact density

By assuming that the buoyancy component of each contact force does not depend on S, it directly implies that any change with S comes from a change in contact structure. This could have been either a change in c_ρ, P_E, or the contact force vector $\boldsymbol{n}_c$. As we have seen in the previous section the contact density c_ρ is the sole culprit.

The scaling of c_ρ with S can be understood by considering the contact between a bulk particle and the intruder. An area A_s on the surface of the intruder is shielded from having contacts with
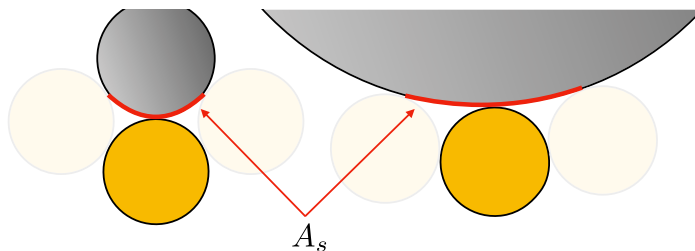
FIG. 3. Two-dimensional schematic depicting the decrease in curvature and increase of the shielded area A_s [71,72] when the intruder size ratio increases. As a result the contact density decreases with size ratio.

other bulk particles [71,72] (see Fig. 3). In three dimensions A_s is given by

$$A_s = 2\pi S^2 r_b^2 \left(1 - \sqrt{1 - \left(\frac{1}{S+1}\right)^2} \right),$$ (21)

where $r_b = d_b/2$. The limits $A_s(S=1)/r_b^2 = 2\pi(1 - \sqrt{3/4}) \approx 0.84$ and $A_s(S \to \infty)/r_b^2 = \pi$ tell us that A_s increases with S. To relate the contact density to A_s we recall a property called the compacity $c_s \equiv \mathcal{Z}A_s/A_p = A_s c_\rho$. Previous studies have assumed and validated that compacity is roughly constant for larger particles in compressed polydisperse packings [71–73]. If the same assumption is used here, then the contact density could be expressed as $c_\rho(S) = c_s/A_s(S)$, and the decrease of contact density with size ratio can be rationalized through an increase in shielded area. Another way of thinking about this is to attribute the scaling of the buoyancy force with size ratio to a decrease in surface curvature of the intruder.

V. RELEVANCE TO MIXTURE THEORY SEGREGATION MODELING

Before concluding this work we will describe briefly a relevant link between the granular buoyancy force derived here and segregation modeling based on the mixture theory framework.

Following the seminal work of Savage and Lun [18], who proposed a statistical mechanical approach to modeling of particle segregation that related microscopic properties to macroscopic segregation velocities, Gray and Thornton [32] introduced an approach based on mixture theory. Like the microscopic models presentation in this paper the continuum mixture theory approach is also built on the assumptions of a linear pressure with depth that is independent of intruder size (see Sec. IV B, assumptions 2 and 3). The mixture theory approach was simpler to follow and has been picked up my many others (see, e.g., Refs. [16,29,34]).

Mixture theory deals with *partial* variables that are defined per unit volume of the mixture rather than *intrinsic* variables associated with properties of the individual constituents. The basic mixture postulate states that every point in the mixture is 'occupied simultaneously by all constituents', and, hence, at each point in space and time there are overlapping partial variables associated with the different constituents [74]. For most variables simple relations can be shown between their intrinsic and partial counterparts. For example, the relationships for density and velocity are, respectively,

$$\rho^\nu = \phi^\nu \rho^{\nu*}, \quad u^\nu = u^{\nu*},$$ (22)

where the superscript * denotes an intrinsic variable. The superscript ν is a place holder for the constituent name, such that summing over the number of constituents n gives the bulk variable:

$$\rho = \sum_{\nu=1}^{n} \rho^\nu.$$ (23)

However, in general, no relationship can be shown between the partial and intrinsic stress of the constituents. For the case where the stress tensor can be represented by a hydrostatic pressure field, it is common to assume a linear volume fraction scaling for the pressure as well, that is,

$$p^v = \phi^v p^{v*}. \tag{24}$$

For granular segregation a relation like Eq. (24) had to be generalized with

$$p^v = f^v p, \tag{25}$$

where f was postulated (see Ref. [21] for a review of proposed forms for f). Interestingly, Archimedes' principle can be used to show that Eq. (24) holds for a fluid constituent interacting with a solid constituent [75]. Thus, theoretically, an Archimedes' principle for one granular constituent submerged in another, like the one presented in this work, could be used to derive Eq. (24) for granular materials.

Recently, Ref. [76] showed how to bridge this gap between the microscopic description presented in Secs. I–IV and the macroscopic description presented here. However, they did not get perfect agreement when upscaling a single particle model to predict a system with a more equal volume fraction ϕ. We would suggest they are missing extra forces which arise when multiple large particles interact. Therefore, extra work is still required on the microscopic description before it can be used to create a predictive macroscopic model. However [76] shows clearly how the two descriptions can be linked. Therefore, in the future it will be possible to have a continuum model which is closed in terms of microscopic particle parameters.

VI. CONCLUSIONS

We have derived and verified a micromechanical based definition for the granular buoyancy force on a single grain in a dense granular flow. The definition is micromechanical in the sense that it takes into account both the structure of contacts and forces on the grain. This granular buoyancy force differs from classic Archimedean buoyancy in two ways. When a grain is identical to the surrounding bulk particles the buoyancy force is balanced by gravity. But when the grain becomes larger than the bulk particles the buoyancy force becomes less than the gravitational force and asymptotically approaches classic Archimedean buoyancy.

We also report that the scaling of granular buoyancy with the size ratio between the intruder grain and bulk particles can be attributed entirely to a change in contact density. This simple but important insight sheds new light on the micromechanical behavior of granular buoyancy. The scaling of contact density with intruder size effects the total force and also each of its components, such as lift and drag forces.

The granular buoyancy derived here lends additional support to a recent study on the lift force experienced by segregating large intruders [44]. The insights into the segregation lift force that were reported, and are more firmly established through the current study, are as follows: first, granular buoyancy does not balance the weight of large segregating intruders and thus the segregation lift force is obtained by subtracting this buoyancy force from the total vertical contact force [44]. Furthermore, the segregation lift force has a maximum and decreases for large size ratios.

We have compared the micromechanical definition to the previously reported Voronoi-based approximation [44] of the granular buoyancy force. We find that the new definition and the approximation yield very similar results and tend to the correct limits. The Voronoi-based approximation does overestimate the micromechanical definition above a size ratio of 2. From a practical point of view, the micromechanical definition should be more accurate but it is more challenging to measure. While the purely geometrical Voronoi-based approximation, however, sacrifices a physical and theoretical foundation for ease of measurement [44].

Future work could investigate at what exact size ratio the classic Archimedean buoyancy is approached by measuring the vertical component of the total contact force experienced by very large freely sinking intruders. We have briefly described how the derived granular buoyancy force could

play a role in further development of segregation models based on mixture theory [17,29,32,34,35], using the approach described by Ref. [76]. This approach would reveal how the idea of a granular buoyancy arises in these different mixture theory descriptions and how the different modeling approaches can be interrelated and combined. Ultimately, leading to a connection between the micro and macro descriptions of segregation. Last, we verified the micromechanical definition of granular buoyancy for mono-disperse flows. Although there is no obvious reason to believe that this definition does not hold for polydisperse flows, this should be investigated nonetheless.

ACKNOWLEDGMENTS

APPENDIX A: CALCULATING PARAMETERS FROM RAW DATA

In this Appendix, several equations are defined that are used for calculating parameters in the main text and the other appendices. To distinguish several parameters that are measured in the simulations from their theoretical definitions in the main text we use the hat (ˆ) symbol.

The contact structure, or the average local number of contacts per area in area element ΔA_{ij}, is given by

$$\hat{E}_{ij} = \frac{1}{N_t \Delta A_{ij}} \sum_c 1, \quad c \in \Delta A_{ij}, \tag{A1}$$

where the contact c needs to be within element ΔA_{ij}. Summation over the surface area yields the coordination number

$$\mathcal{Z} = \sum_i \sum_j \hat{E}_{ij} \Delta A_{ij}. \tag{A2}$$

The average local force on a surface element $\hat{\boldsymbol{F}}_{ij}$ can be obtained by summation of all local contact forces $\hat{\boldsymbol{f}}_c$,

$$\hat{\boldsymbol{F}}_{ij} = \frac{1}{N_t} \sum_c \hat{\boldsymbol{f}}_c, \quad c \in \Delta A_{ij}. \tag{A3}$$

Note that summing over all elements yields the average net or total contact force on the intruder,

$$\hat{\boldsymbol{F}}_{tot} = \sum_i \sum_j \hat{\boldsymbol{F}}_{ij}. \tag{A4}$$

The force structure or average contact force $\hat{\boldsymbol{F}}_{c_{ij}}$ in a single element ΔA_{ij} is obtained by dividing the average local force by the number of contacts,

$$\hat{\boldsymbol{F}}_{c_{ij}} = \frac{\hat{\boldsymbol{F}}_{ij}}{\hat{E}_{ij} \Delta A_{ij}}. \tag{A5}$$

The average total force on the intruder particle can also be expressed as

$$\hat{\boldsymbol{F}}_{tot} = \sum_i \sum_j \hat{\boldsymbol{F}}_{c_{ij}} \hat{E}_{ij} \Delta A_{ij}. \tag{A6}$$

We make use of the time-averaged number of contacts on a surface element,

$$C_{ij} = \frac{1}{N_t} \sum_c 1, \quad c \in \Delta A_{ij}, \tag{A7}$$
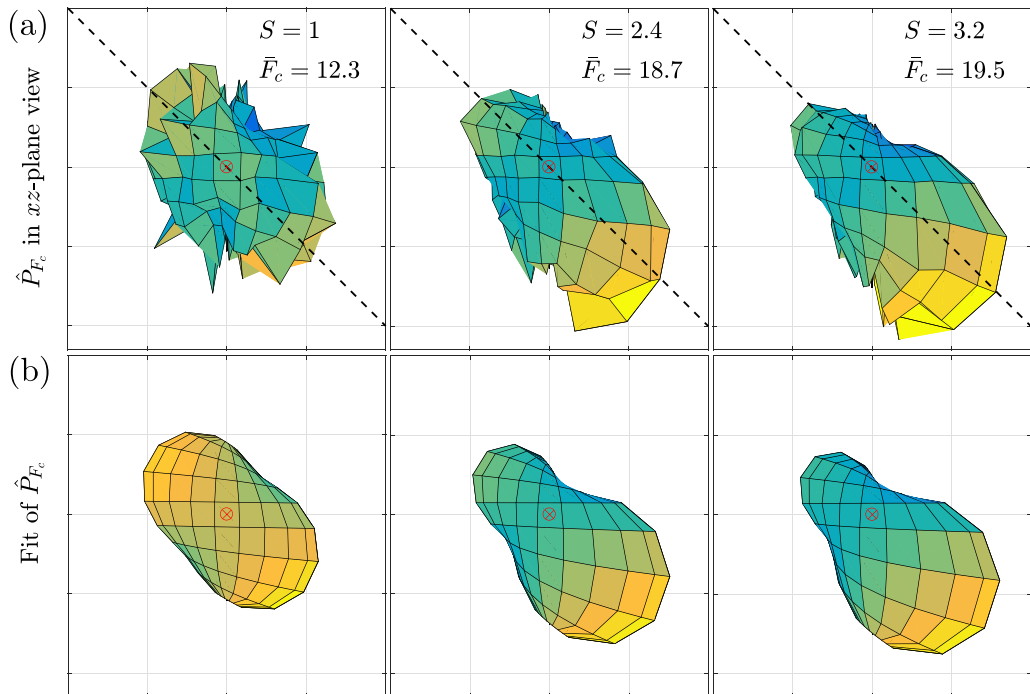
FIG. 4. (a) Upper row shows a measurement of the normalized angular distribution of the contact force P_{F_c} on an intruder for increasing S on equal grids and in the xz plane. The red cross marks the center of the plot. Dashed lines are visual guides. The average contact force is also shown in each panel. (b) Bottom row shows fits to the measured data using Eq. (B1). The color bar for all plots are identical.

to calculate the three-dimensional normalized angular distribution of forces $\hat{P}_{F_c}$ we use

$$\hat{P}_{F_c,ij} = \frac{|\hat{\boldsymbol{F}}_{ij}|}{C_{ij}} \frac{A_p}{\sum_i \sum_j \frac{|\hat{\boldsymbol{F}}_{ij}|}{C_{ij}} \Delta A_{ij}}, \tag{A8}$$

where $|...|$ indicates the vector norm. The three-dimensional normalized contact distribution of forces $\hat{P}_E$ is calculated using

$$\hat{P}_{E,ij} = \frac{C_{ij}}{\Delta A_{ij}} \frac{A_p}{\sum_i \sum_j C_{ij}}. \tag{A9}$$

APPENDIX B: MEASURING THE ANGULAR DISTRIBUTION FUNCTIONS

1. Force distribution

Figure 4(a) shows measurements of the three-dimensional normalized angular distribution of forces $\hat{P}_{F_c}$, viewed in the xz-plane, for three different intruder size ratios. These are calculated using Eq. (A8). The average contact force $\bar{F}_c$ is also shown and increases with S. The distribution for $S = 1$ is pill-shaped and angled at $45°$. As S increases this shape changes and contact forces at the bottom-right corner grow with respect to the top-left corner. This matches previous observations of an increase in pressure at the bottom of the intruder on the downstream side in combination with an increase in anisotropy [44]. Readers should not be mislead to believe that forces at the top-left are decreasing with S. After all, the distribution is normalized and the average contact force increases.
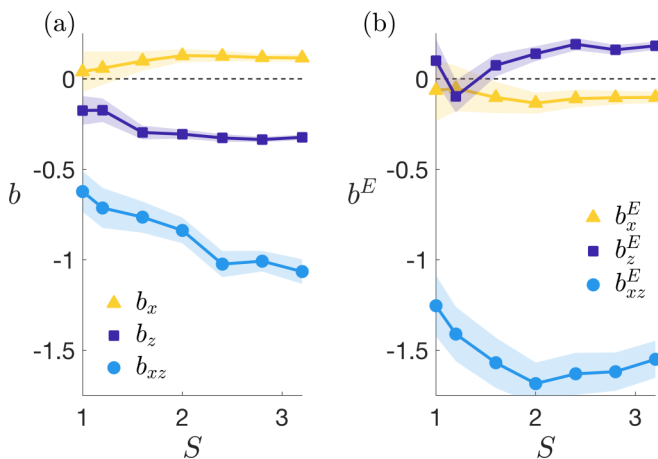
FIG. 5. (a) Coefficients obtained from fitting Eq. (B1) to $\hat{P}_{F_c}$. (b) Coefficients obtained from fitting Eq. (B2) to $\hat{P}_E$. The error bars indicate the 95% confidence intervals of the fitting coefficient.

The force distribution is also but half of the story, the other part is the contact distribution, and together these make up the total contact force felt by the intruder.

The angular distribution of forces can be fitted with an equation combining the most important contribution from a second-order Fourier series [70] and linear contributions for the x and z direction,

$$\hat{P}_{F_c} \approx 1 + b_x r_p \cos(\theta) \sin(\phi) + b_z r_p \cos(\phi) + b_{xz} \cos(\phi) \cos(\theta) \sin(\phi), \qquad (B1)$$

here the right-most term with b_{xz} is responsible for the closed shape of the distribution and for the anisotropy at 45°. This term is nonlinear in the x and z direction but symmetric. The more negative this term is the stronger will be the forces at the top left and bottom right relative to the two other corners. The first and second terms, with b_x and b_z, are horizontal and vertical linear gradients, respectively, and therefore asymmetric. The fits, shown in Figure 4(b), capture the overall shape of the distribution quite well whilst ignoring the noise. The accuracy of the fit is tested in Appendix B 3.

A detailed look at the scaling of the coefficients as a function of S [see Fig. 5(a)] reveals more about the change of the distribution. For $S = 1$ the coefficient b_x is zero, indicating that there is no gradient along the horizontal axis. Coefficient b_z, however, has a small negative value accounting for a linear increase of forces towards the bottom of the particle. For larger size ratios the coefficient b_x grows positively and b_z grows negatively. The latter can be associated with an increase in buoyancy force and emergence of the segregation lift force. The degree of anisotropy, captured by b_{xz}, also grows with S.

Given our assumptions about the buoyancy force in Sec. IV B we take b_z at $S = 1$ for our decomposition of the total force into buoyancy and other forces. We do not take b_{xz} because it is not linear in z.

2. Contact distribution

Figure 6(a) shows measurements of the three-dimensional normalized contact distribution of forces $\hat{P}_E$, viewed in the xz plane, for three different intruder size ratios. These distributions are calculated using Eq. (A9). The contact density c_ρ is also shown and decreases with S. We observe that for all S the top-left and bottom-right part of the intruder encounter many contacts, whilst the top-right and bottom-left barely show any contact. For $S = 1$, two contact planes are visible, one horizontal and a second at an angle of roughly 45° with a dip in contacts in-between
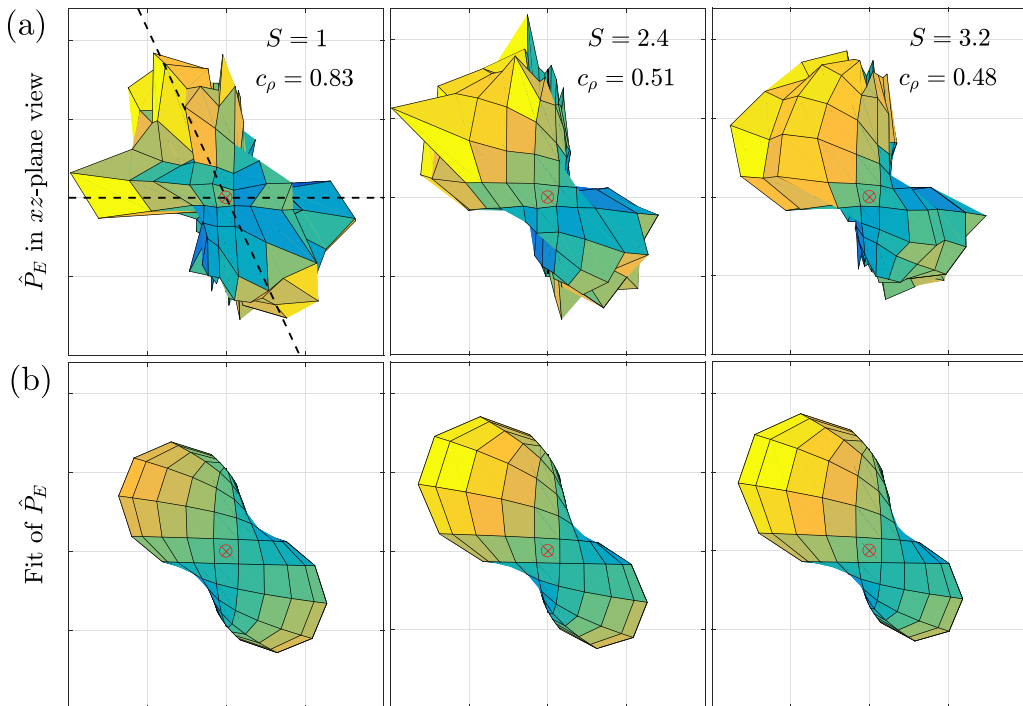
FIG. 6. (a) Upper row shows a measurement of the normalized angular distribution of the number of contacts per surface area P_E on an intruder for increasing S on equal grids and in the xz-plane. The red cross marks the center of the plot. Dashed lines are visual guides. The average contact density is also shown in each panel. (b) Bottom row shows fits to the measured data using Eq. (B2). The color bar for all plots are identical.

them at $22°$. This pattern can be rationalized as follows, the contacts made with particles exactly in front and behind the intruder shield contacts slightly above and below thus resulting in the dip. For $S > 1$ the dip is smoothed out, presumably because contacts can be more evenly distributed along the $45°$ angle. The amount of contacts at the top-left also increases with respect to the bottom-right.

For completeness we also fit the contact distribution. We use a similar fit function as used for $\hat{P}_{F_c}$ but normalized by the intruder surface area,

$$\hat{P}_E \approx 1 + b_x^E r_p \cos(\theta) + b_z^E r_p \cos(\phi) \sin(\phi) + b_{xz}^E \cos(\phi) \cos(\theta) \sin(\phi), \qquad (B2)$$

where r_p is the intruder radius. Similar to Eq. (B2) the right-most term is responsible for anisotropy and the closed shape, whilst the first and second term account for horizontal and vertical gradients, respectively. The fit function is able to capture the overall shape and trend [Fig. 6(b)], although by construction it cannot reproduce the dip in contacts at $22°$ for $S = 1$. The coefficients of the fit as a function of S are shown in Fig. 5(b).

3. Accuracy of the fit functions

We test the accuracy of the fit functions by computing the total force via Eq. (A6) using the fits for the force and contact distributions. A comparison of the vertical component of the total force F_{tot_z} is shown in Fig. 7. Using both fits (light blue curve) the result shows significant deviations from F_z, especially close to $S = 1$. Judging from Fig. 6 it is likely that the fit to P_E is responsible for this. When the raw data for P_E is used instead, the blue curve is obtained, which is
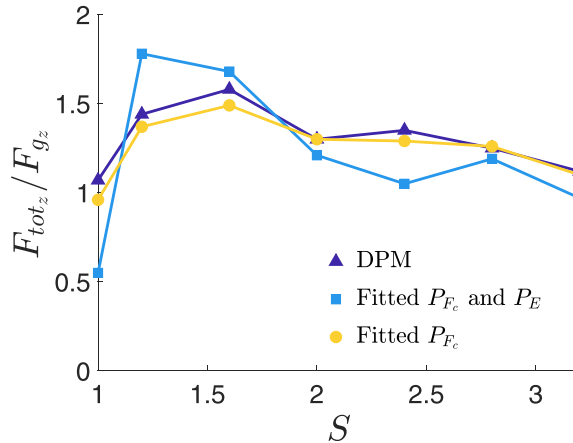
FIG. 7. Vertical component of the total force on the intruder (normalized by gravity) obtained in three different ways; the raw measured value (dark blue triangles), the value calculated using the fits for both P_{F_c} and P_E (light blue squares), and using only the fit for P_{F_c} (yellow circles). In the latter case the raw measured values for P_E are used.

a much better match demonstrating that the fit to P_{F_c} is accurate, whereas P_E is captured much less accurately.

---

[1] I. S. Aranson and L. S. Tsimring, Patterns and collective behavior in granular media: Theoretical concepts, Rev. Mod. Phys. **78**, 641 (2006).

[2] J. M. Ottino and D. V. Khakhar, Mixing and segregation of granular materials, Annu. Rev. Fluid. Mech. **32**, 55 (2000).

[3] J. A. Drahun and J. Bridgwater, The mechanisms of free surface segregation, Powder Technol. **36**, 39 (1983).

[4] J. C. Williams, The segregation of particulate materials: A review, Powder Technol. **15**, 245 (1976).

[5] L. B. H. May, L. A. Golick, K. C. Phillips, M. Shearer, and K. E. Daniels, Shear-driven size segregation of granular materials: Modeling and experiment, Phys. Rev. E **81**, 051301 (2010).

[6] A. Rosato, K. J. Strandburg, F. Prinz, and R. H. Swendsen, Why the Brazil Nuts are on Top: Size Segregation of Particulate Matter by Shaking, Phys. Rev. Lett. **58**, 1038 (1987).

[7] J. Duran, T. Mazozi, E. Clément, and J. Rajchenbach, Size segregation in a two-dimensional sandpile: Convection and arching effects, Phys. Rev. E **50**, 5138 (1994).

[8] J. B. Knight, H. M. Jaeger, and S. R. Nagel, Vibration-Induced Size Separation in Granular Media: The Convection Connection, Phys. Rev. Lett. **70**, 3728 (1993).

[9] D. A. Huerta and J. C. Ruiz-Suárez, Vibration-Induced Granular Segregation: A Phenomenon Driven by Three Mechanisms, Phys. Rev. Lett. **92**, 114301 (2004).

[10] C. R. K. Windows-Yule, T. Weinhart, D. J. Parker, and A. R. Thornton, Influence of thermal convection on density segregation in a vibrated binary granular system, Phys. Rev. E **89**, 022202 (2014).

[11] C. R. K. Windows-Yule, T. Weinhart, D. J. Parker, and A. R. Thornton, Effects of Packing Density on the Segregative Behaviors of Granular Systems, Phys. Rev. Lett. **112**, 098001 (2014).

[12] GDR-MiDi, On dense granular flows, Eur. Phys. J. E **14**, 341 (2004).

[13] P. Jop, Y. Forterre, and O. Pouliquen, A constitutive law for dense granular flows, Nature (London) **441**, 727 (2006).

[14] J. M. Ottino and D. Khakhar, Fundamental research in heaping, mixing, and segregation of granular materials: Challenges and perspectives, Powder Technol. **121**, 117 (2001).

[15] L. A. Golick and K. E. Daniels, Mixing and segregation rates in sheared granular materials, Phys. Rev. E **80**, 042301 (2009).

[16] Y. Fan and K. M. Hill, Shear-driven segregation of dense granular mixtures in a split-bottom cell, Phys. Rev. E **81**, 041303 (2010).

[17] Y. Fan and K. M. Hill, Theory for shear-induced segregation of dense granular mixtures, New J. Phys. **13**, 095009 (2011).

[18] S. B. Savage and C. K. K. Lun, Particle size segregation in inclined chute flow of dry cohesionless granular solids, J. Fluid Mech. **189**, 311 (1988).

[19] K. M. Hill and D. S. Tan, Segregation in dense sheared flows: Gravity, temperature gradients, and stress partitioning, J. Fluid Mech. **756**, 54 (2014).

[20] L. Staron and J. C. Phillips, Stress partition and microstructure in size-segregating granular flows, Phys. Rev. E **92**, 022210 (2015).

[21] D. R. Tunuguntla, T. Weinhart, and A. R. Thornton, Comparing and contrasting size-based particle segregation models, Comp. Part. Mech. **4**, 387 (2017).

[22] S. Wiederseiner, N. Andreini, G. Épely-Chauvin, G. Moser, M. Monnereau, J. M. N. T. Gray, and C. Ancey, Experimental investigation into segregating granular flows down chutes, Phys. Fluids **23**, 013301 (2011).

[23] C. G. Johnson, B. P. Kokelaar, R. M. Iverson, M. Logan, R. G. LaHusen, and J. M. N. T. Gray, Grain-size segregation and levee formation in geophysical mass flows, J. Geophys. Res.: Earth Surf. **117**, F01032 (2012).

[24] L. Staron and J. C. Phillips, Segregation time-scale in bi-disperse granular flows, Phys. Fluids **26**, 033302 (2014).

[25] M. Harrington, J. H. Weijs, and W. Losert, Suppression and Emergence of Granular Segregation Under Cyclic Shear, Phys. Rev. Lett. **111**, 078001 (2013).

[26] A. N. Edwards and N. M. Vriend, Size segregation in a granular bore, Phys. Rev. Fluids **1**, 064201 (2016).

[27] B. Marks, J. A. Eriksen, G. Dumazer, B. Sandnes, and K. J. Måløy, Size segregation of intruders in perpetual granular avalanches, J. Fluid Mech. **825**, 502 (2017).

[28] A. Tripathi and M. Nema, Size segregation of binary granular mixtures-towards more appropriate scaling of percolation velocity, EPJ Web Conf. **140**, 03082 (2017).

[29] A. M. Fry, P. B. Umbanhowar, J. M. Ottino, and R. M. Lueptow, Effect of pressure on segregation in granular shear flows, Phys. Rev. E **97**, 062906 (2018).

[30] A. M. Fry, P. B. Umbanhowar, J. M. Ottino, and R. M. Lueptow, Diffusion, mixing, and segregation in confined granular flows, AIChE J. **65**, 875 (2019).

[31] R. Cai, H. Xiao, J. Zheng, and Y. Zhao, Diffusion of size bidisperse spheres in dense granular shear flow, Phys. Rev. E **99**, 032902 (2019).

[32] J. M. N. T. Gray and A. R. Thornton, A theory for particle size segregation in shallow granular free-surface flows, Proc. R. Soc. A. **461**, 1447 (2005).

[33] A. R. Thornton, J. M. N. T. Gray, and A. J. Hogg, A three-phase mixture theory for particle size segregation in shallow granular free-surface flows, J. Fluid Mech. **550**, 1 (2006).

[34] B. Marks, P. Rognon, and I. Einav, Grainsize dynamics of polydisperse granular segregation down inclined planes, J. Fluid Mech. **690**, 499 (2012).

[35] D. R. Tunuguntla, O. Bokhove, and A. R. Thornton, A mixture theory for size and density segregation in shallow granular free-surface flows, J. Fluid Mech. **749**, 99 (2014).

[36] P. B. Umbanhowar, R. M. Lueptow, and J. M. Ottino, Modeling segregation in granular flows, Annu. Rev. Chem. Biomol. Eng. **10**, 129 (2019).

[37] Y. Liu, M. Gonzalez, and C. Wassgren, Modeling granular material segregation using a combined finite element method and advection–diffusion–segregation equation model, Powder Technol. **346**, 38 (2019).

[38] K. van der Vaart, P. Gajjar, G. Epely-Chauvin, N. Andreini, J. M. N. T. Gray, and C. Ancey, Underlying Asymmetry within Particle Size Segregation, Phys. Rev. Lett. **114**, 238001 (2015).

[39] P. Gajjar and J. M. N. T. Gray, Asymmetric flux models for particle-size segregation in granular avalanches, J. Fluid Mech. **757**, 297 (2014).

[40] Tunuguntla, Deepak R. and Thornton, Anthony R., Balancing size and density segregation in bidisperse dense granular flows, EPJ Web Conf. **140**, 03079 (2017).

[41] L. Staron and J. C. Phillips, How large grains increase bulk friction in bi-disperse granular chute flows, Comp. Part. Mech. **3**, 367 (2016).

[42] L. Jing, C. Y. Kwok, and Y. F. Leung, Micromechanical Origin of Particle Size Segregation, Phys. Rev. Lett. **118**, 118001 (2017).

[43] F. Guillard, Y. Forterre, and O. Pouliquen, Scaling laws for segregation forces in dense sheared granular flows, J. Fluid Mech. **807**, R1 (2016).

[44] K. van der Vaart, M. van Schrojenstein Lantman, T. Weinhart, S. Luding, C. Ancey, and A. Thornton, Segregation of large particles in dense granular flows suggests a granular Saffman effect, Phys. Rev. Fluids **3**, 074303 (2018).

[45] L. Staron, Rising dynamics and lift effect in dense segregating granular flows, Phys. Fluids **30**, 123303 (2018).

[46] L. Jing, J. M. Ottino, R. M. Lueptow, and P. B. Umbanhowar, Rising and sinking intruders in dense granular flows, Phys. Rev. Research **2**, 022069(R) (2020).

[47] G. Félix and N. Thomas, Evidence of two effects in the size segregation process in dry granular media, Phys. Rev. E **70**, 051307 (2004).

[48] G. Hill, S. Yeung, and S. A. Koehler, Scaling vertical drag forces in granular media, Europhys. Lett. **72**, 137 (2005).

[49] P. G. T. Saffman, The lift on a small sphere in a slow shear flow, J. Fluid Mech. **22**, 385 (1965).

[50] A. Kumar, D. V. Khakhar, and A. Tripathi, Theoretical calculation of the buoyancy force on a particle in flowing granular mixtures, Phys. Rev. E **100**, 042909 (2019).

[51] The sign convention of stress in the granular material community and the fluids community is different. In this work the fluid convention is adopted where compressional stress is negative.

[52] T. Weinhart, R. Hartkamp, A. R. Thornton, and S. Luding, Coarse-grained local and objective continuum description of three-dimensional granular flows down an inclined surface, Phys. Fluids **25**, 070605 (2013).

[53] D. A. Huerta, V. Sosa, M. C. Vargas, and J. C. Ruiz-Suárez, Archimedes' principle in fluidized granular systems, Phys. Rev. E **72**, 031307 (2005).

[54] We suspect that the imbalance between gravity and buoyancy is the reason why Huerta *et al.* [53] chose to use intruders of lesser density than the bulk particles. Intruders of the same density would likely have sunken, which, given their experimental design to measure net upward forces, was perhaps something they were not looking for.

[55] M. E. Möbius, B. E. Lauderdale, S. R. Nagel, and H. M. Jaeger, Brazil-nut effect: Size separation of granular particles, Nature (London) **414**, 270 (2001).

[56] W. Kang, Y. Feng, C. Liu, and R. Blumenfeld, Archimedes' law explains penetration of solids into granular media, Nat. Commun. **9**, 1 (2018).

[57] Y. Feng, R. Blumenfeld, and C. Liu, Support of modified archimedes' law theory in granular media, Soft Matter **15**, 3008 (2019).

[58] N. Thomas, Reverse and intermediate segregation of large beads in dry granular media, Phys. Rev. E **62**, 961 (2000).

[59] G. Mansoori, N. F. Carnahan, K. Starling, and T. Leland Jr, Equilibrium thermodynamic properties of the mixture of hard spheres, J. Chem. Phys. **54**, 1523 (1971).

[60] L. E. Silbert, D. Ertaş, G. S. Grest, T. C. Halsey, D. Levine, and S. J. Plimpton, Granular flow down an inclined plane: Bagnold scaling and rheology, Phys. Rev. E **64**, 051302 (2001).

[61] T. Weinhart, A. R. Thornton, S. Luding, and O. Bokhove, Closure relations for shallow granular flows from particle simulations, Granular Matter **14**, 531 (2012).

[62] P. A. Cundall and O. D. L. Strack, A discrete numerical model for granular assemblies, Geotechnique **29**, 47 (1979).

[63] S. Luding, Cohesive, frictional powders: Contact models for tension, Granular Matter **10**, 235 (2008).

[64] A. R. Thornton, T. Weinhart, V. Ogarko, and S. Luding, Multiscale method for multi-component granular materials, Comput. Methods Mater. Sci. **13**, 197 (2013).

[65] T. Weinhart, D. R. Tunuguntla, M. P. van Schrojenstein-Lantman, A. J. van der Horn, I. F. C. Denissen, C. R. Windows-Yule, A. C. de Jong, and A. R. Thornton, MercuryDPM: A fast and flexible particle solver Part A: Technical advances, in *Proceedings of the 7th International Conference on Discrete Element Methods* (Springer, Singapore, 2017), pp. 1353–1360.

[66] T. Weinhart, L. Orefice, M. Post, M. P. van Schrojenstein Lantman, I. F. Denissen, D. R. Tunuguntla, J. Tsang, H. Cheng, M. Y. Shaheen, H. Shi, P. Rapino, E. Grannonio, N. Losacco, J. Barbosa, L. Jing, J. E. A. Naranjo, S. Roy, W. K. den Otter, and A. R. Thornton, Fast, flexible particle simulations—An introduction to mercuryDPM, Comput. Phys. Commun. **249**, 107129 (2020).

[67] L. Rothenburg and R. Bathurst, Analytical study of induced anisotropy in idealized granular materials, Geotechnique **39**, 601 (1989).

[68] F. Radjai, D. E. Wolf, M. Jean, and J.-J. Moreau, Bimodal Character of Stress Transmission in Granular Packings, Phys. Rev. Lett. **80**, 61 (1998).

[69] N. P. Kruyt and L. Rothenburg, Kinematic and static assumptions for homogenization in micromechanics of granular materials, Mech. Mater. **36**, 1157 (2004).

[70] H. Ouadfel and L. Rothenburg, Stress–force–fabric relationship for assemblies of ellipsoids, Mech. Mater. **33**, 201 (2001).

[71] M. R. Shaebani, M. Madadi, S. Luding, and D. E. Wolf, Influence of polydispersity on micromechanics of granular materials, Phys. Rev. E **85**, 011301 (2012).

[72] M. Madadi, O. Tsoungui, M. Lätzel, and S. Luding, On the fabric tensor of polydisperse granular materials in 2D, Int. J. Solids Struct. **41**, 2563 (2004).

[73] F. Göncü, O. Durán, and S. Luding, Constitutive relations for the isotropic deformation of frictionless packings of polydisperse spheres, C. R. Mec. **338**, 570 (2010), Micromechanics of granular materials.

[74] L. W. Morland, Flow of viscous fluids through a porous deformable matrix, Surv. Geophys. **13**, 209 (1992).

[75] A. Thornton, A study of segregation in granular gravity driven free surface flows, Ph.D. thesis, The University of Manchester, 2005.

[76] H. Rousseau, R. Chassagne, J. Chauchat, R. Maurin, and P. Frey, Bridging the gap between particle-scale forces and continuum modeling of size segregation: Application to bedload transport, J. Fluid Mech. **916**, A26 (2021).